WOOD RESEARCH doi.org/10.37763/wr.1336-4561/68.1.112128
ISSN 1336-4561 e-ISSN 2729-8906
68(1): 2023 112-128 pp.

EXPERIMENTAL ANALYSIS OF ACOUSTIC EMISSION PROPAGATION VELOCITIES AND ENERGY ATTENUATION LAW OF P AND S WAVES IN WOOD USING IMPROVED TDOA MEASUREMENTS

SAIYIN FANG[1], MING LI[2,3], WEI LI[1], CHANG LIN HUANG[1], TINGTING DENG[1], KUN DU[1]

[1]SOUTHWEST FORESTRY UNIVERSITY, CHINA
[2]KEY LABORATORY OF ADVANCED PERCEPTION AND INTELLIGENT CONTROL OF HIGH-END EQUIPMENT OF MINISTRY OF EDUCATION
[3]ANHUI POLYTECHNIC UNIVERSITY, CHINA

(RECEIVED JUNE 2022)

ABSTRACT

To explore the propagation law of AE signal in wood, the propagation velocity of P-wave and S-wave and the energy attenuation law of different frequency components were studied By PLB (pencil-lead break) tests. Firstly, an improved time-difference-of-arrival (TDOA) method was designed to determine the arrive time. The propagation velocities of P-wave and S-wave were calculated. Then, the Young's modulus was estimated by P-wave velocity. Finally, on the basis of eliminating the influence of standing wave, the energy attenuation models were obtained by numerical fitting and wavelet decomposition. The results showed that the improved TDOA algorithm can calculate the propagation velocity of P-wave and S-wave at the same time through one test, and the P-wave velocity can be used to estimate the Young's modulus. P-wave propagated faster in soft wood, while S-wave propagated faster in hard wood. The higher the frequency of AE signal, the faster the energy attenuation.

KEYWORDS: AE, wood, P-wave, S-wave, propagation characteristic.

INTRODUCTION

As a promising structural health monitoring (SHM) method developed in recent years, acoustic emission technique (AET) has increasingly played an important role in damage mechanism identification and classification, damage source localization and severity assessment, owing to its dynamic and continuous monitoring of the damage initiation and evolution in real time (Wu et al. 2020, Pallarés et al. 2021). Despite the widespread use of AET to characterize and monitor the damage evolution of metal, rock and composite materials, only a few research

studies have focused on wood materials (Lamy et al. 2015). Due to lack of comprehensive understanding of AE characteristics, AET only works as an auxiliary qualitative approach to SHM of wood structures.

A typical application of AET in wood is monitoring and examining its fracture process. Reiterer et al. (2000) studied the mode I fracture behavior in the radial-longitudinal (RL) crack propagation system of two softwoods and three hardwoods by monitoring AE activity. The finding indicated that the fracture behavior appearing in two kinds woods could be distinguished though the parameters of cumulative counts, amplitudes and frequency spectra of the emitted AE events. Aicher et al. (2001) studied the AE characteristics during the failure of spruce in tension perpendicular to grain, and the investigations revealed that the correlation of AE event rates with global strain allowed a tracing of the damage evolution. For this reason, the authors thought that AE signals can be taken as damage indicators of progressive damage. Ando et al. (2006) used the generation characteristics of AE events to examine the unique micro fracture process of old wood. The results showed that the AE events released in old wood were more than that in new one under lighter load, but the amplitudes were smaller. AE was also used to monitor the failure process of hardwood and softwood under static and fatigue torsional loading (Chen et al. 2006). The experimental results showed that AE activities indicated some micro-crack initiation before the visible cracking under torsional-loading. Specially, hardwood produced more AE counts than softwood during testing. Ristcel et al. (2013, 2014) studied the characteristics of AE activities generated in solid wood and laminated veneer lumber (LVL) under tensile tests. The experimental results indicated that at stress levels below 50%, although the specimen surface had no obvious crack, the AE signals had been able to detect the early internal damage. Specially, the AE counts released from LVL was less than that from solid wood but the strength was greater. The accumulative AE events increased exponentially with time in LVL but that increased linearly in solid wood specimens. Ohuchi et al. (2011) measured the AE generated during the compact tension tests of sugi specimens. The mainly conclusion was that the peaks in the AE were admitted in the fracture process of the specimen and it corresponded to the position of the late wood part in progressing the crack. Lamy et al. (2015) used a double cantilever beam specimen to study the open mode behavior of Douglas fir wood samples. The experiment showed that crack initiation and crack growth detected by AE activities was in a good agreement with the image analysis results. AE events had also been used to predict the crack length of wood at different relative humidity (Bertolin et al. 2020). Recently, Hu et al. (2022) studied the effects of growth rings in terms of crack tip locations (at earlywood, early-latewood, and latewood) on the AE characteristic signals of souther yellow pine through testing CT (compact tension) blocks in RL cracking propagation system. Experimental results indicated that the crack tip location had significant effects on counts and energy but not the amplitude of AE. In addition, AET has been used in wood cutting processing (Aguilera et al. 2007, Nasir et al. 2018, 2020), wood thermal modification (Nasir et al. 2018, 2019, 2019a) and wood defect identification (Sun et al. 2008, 2013, Wang et al. 2020).

The parameters such as AE counts, cumulative number of AE events, AE amplitude and so on, directly provided by the AE instruments were adopted to analysis qualitatively the processes of wood damage or fracture in the previous literature. In fact, all the characteristic information of

AE activities is contained in the waveform. Particularly, the most important concerns are to know exactly when and damages appear, making it necessary to precisely characterize the AE wave propagation property, including wave attenuation and velocity (Michalocova et al. 2018). Unfortunately, comparison to the application of AE parameters, gaining and analysis of AE waveform were lack of attention in the field of wood science and technology. Wavelet transform (Li et al. 2018, 2021) and empirical mode decomposition (EMD) (Li et al. 2019) methods were used to reconstruct AE waveform from original noisy collection data. On the base of AE waveforms, Li et al. (2018) used signal cross-correlation analysis method to determine the TDOA of the different sensors. Meanwhile, such TDOA was used to calculate the velocity of AE wave propagating on the surface of the wood specimen. Similarly, Li et al. (2020) used TDOA to evaluate the propagation velocities of AE waves on the surface of wood specimens with different MC from 0 to 123.4%. the studies showed that the velocity of AE waves decreased rapidly when MC was below FSP (fiber saturation point), and decreased relatively gently when the MC was above FSP. More recently, Li et al. (2021) designed a combined method of wavelet and cross-correlation analyses to reconstruct the AE waveform from the original signals propagated in wood specimens. Then, TDOA was used to calculate the velocity of STW (surface transverse wave) and ILW (internal longitudinal wave) by different tests. the results showed that the propagation velocity of ILW was about 4.6 times that of STW in the same species of wood.

As mentioned above, some fundamental characteristics of AE waveform such as propagation mode, propagation velocity, energy attenuation and so on, are the keys for AET application in wood and wood structure. Because the propagation of AE wave travelling in the earth is very similar to that in wood materials, an AE wave is divided into three parts, P wave, S wave and stationary wave in this paper, where, P and S wave have the similar definition as that in seismology. The stationary wave component can be regarded as a kind of steady-state solution of wave equation of AE propagating in wood. Considering the effect of species, the wood specimens were made from two different wood materials in this paper, one was *Pinus sylvestris var. Mongolicas Litv*, a kind of coniferous wood and the other was *Zelkova schneideriana*, a kind of broadleaf wood. Then, improved TDOA approaches with adaptive threshold (TDOA-ah) were built for P and S waves respectively. With TDOA-ah methods, two propagation velocities of P and S waves were calculated under different distances. In addition, the propagation velocities were used to estimate the Yang's modulus of the specimen. At last, four components were gained by four-layer wavelet transform of an AE wave, energy attenuation process were fitted by exponent function for different components. The aim was to reveal the influence of frequency on energy attenuation.

MATERIAL AND METHODS

Test materials

The difference of wood microstructure can obviously affect the propagation characteristics of AE signal. Therefore, in this paper, *Pinus sylvestris var. Mongolicas Litv.* and *Zelkova schneideriana* sawn timber were used to make tangential specimens. The former belongs to coniferous timber and the latter is typical broad-leaved timber. For the convenience of

description, PS and ZS are used to represent *Pinus sylvestris var. mongolica Litv*. and *Zelkova schneideriana* respectively. Considering the significant attenuation characteristics of AE signal in wood, the size of all specimens was 800 × 100 × 30 mm (Fig. 1b), the densities of PS and ZS specimens were 375 $kg \cdot m^{-3}$ and 696 $kg \cdot m^{-3}$ respectively, and the moisture content was 11.1% and 14.3% respectively. All specimens had straight texture and no defects.

Acquisition of AE signals

In order to obtain complete original AE signal waveform data, an 8-channel AE signal acquisition system was built. The data acquisition equipment was Ni usb-6366 high data acquisition card, which supported a maximum sampling rate of 2M. Li et al. (2017, 2021) research showed that the maximum frequency of wood AE signal did not exceed 200kHz, so the AE sampling frequency in this paper was set to 500 kHz, and the variation range of signal amplitude was (- 5V, 5V). All sensors were Shenghua SR-150N AE sensors, with a resonant frequency of 150 kHz. The output of each sensor was equipped with a 40 dB gain PAI front-end amplifier (Fig. 1a). The AE signal data of each channel was separated and stored through the software platform developed in LabVIEW environment.

Test methods

Considering the inhomogeneity and attenuation characteristics in the AE propagation process, 5 AE sensors ere arranged at equal intervals of 150 mm on a plane of 800 × 100 mm of the specimen and the AE signals collected by each sensor were recorded as s1, s2, s3, s4 and s5 respectively. During the test, the AE sensor and AE source were always kept in the same plane. In order to prevent the signal of the sensor closest to the AE source from clipping distortion. Ensure that the AE source can be transmitted to the farthest sensor, the AE source signal was generated by PLB test at the place 100 mm away from the rightmost AE sensor according to ASTM-E976 standard (Fig. 1b). The specific method was to use a 2H pencil lead with a diameter of 0.5 mm to break the lead at an angle of 30 degrees and a distance of 2.5 mm from the contact point, and 15 independent PLB tests in the same location were carried out on the same specimen.

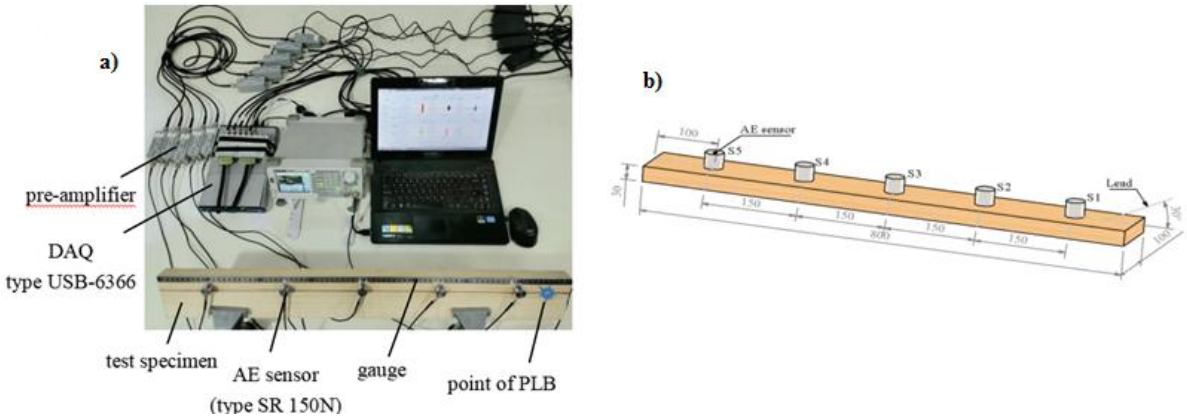

Fig. 1: AE signal collection system: a) Components of the signal collection system, b) Schematic diagram of test piece.

Energy estimation of AE waveform

The energy estimation of AE waveform was based on the elastic wave theory. The waveform of AE signal propagating in the experimental specimen can be divided into three parts: P-wave, S-wave and standing wave (Fig. 2). P-wave is the longitudinal wave that reaches the sensor first, S-wave is the transverse wave that follows the P-wave, and the amplitude of S-wave is significantly higher than that of P-wave. Standing wave is the stable state of AE signal propagating in the specimen. Obviously, the influence of standing wave needs to be avoided when analyzing the attenuation process of AE energy. In fact, in the AE signal waveform in Fig. 2, P-wave and S-wave components dominate in the 0.5 ms range after AE arrival. Therefore, in this paper, the energy of AE waveform was calculated based on the signal within 0.5 ms after P-wave arrival, corresponding to 250 data.

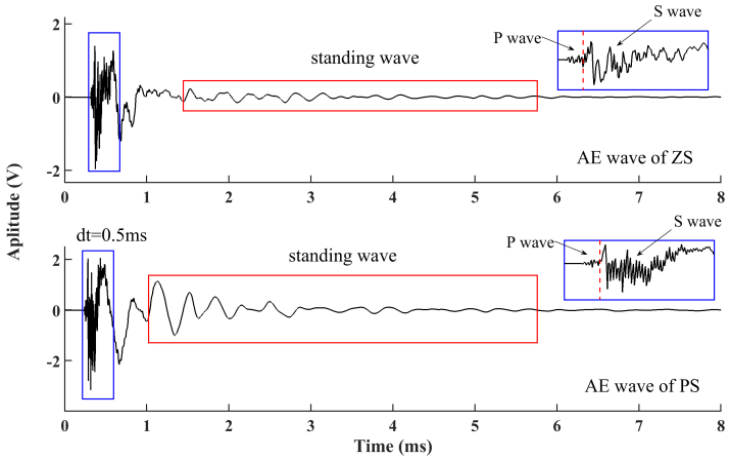

Fig. 2: Original AE signal waveform.

In the analysis of the AE signal energy, the AE signal was considered as an AC current and the heat generated through a 1Ω resistor at a fixed time was taken as the AE signal energy:

$$W = \int_0^t \frac{u^2}{R} d\tau \qquad (1)$$

Since the AE signals collected by the system were discontinuous, Eq.1 is discretized, and the two data are separated by 1/*f* second. Assuming that the Zero-order retainer is used in the discretization process, that is, the signal amplitude remains unchanged during this period, then the AE signal energy is calculated as Eq. 2:

$$W = \sum_{i=1}^{n} \Delta t_i \cdot u_i^2 = nT \sum_{i=1}^{n} u_i^2 \qquad (2)$$

$$\Delta t_i = T = 1/f_s \qquad i = 1,2,...,n$$

where: f_s is the sampling frequency and n is the data length.

P-wave velocity calculation based on improved TDOA algorithm

Approaches based on TDOA measurements from spatially separated sensors are widely used to estimate AE wave velocity because they are more effective than the methods using the other fundamental measurements (Zhou et al. 2021). Because the propagation velocity of longitudinal wave is always greater than that of transverse wave when elastic wave propagates in the same material, the first time to reach the sensor was the P-wave component of the AE signal in this study. Therefore, the arrival time of P-wave can be determined by setting the threshold, that is, the time when AE signal exceeds the set threshold for the first time was recorded as the arrival time of P-wave. However, the AE signal experienced obvious attenuation when propagating in the wood. The farther the sensor was from the AE source, the smaller the amplitude when the P-wave reached, and the amplitude differed by several times. For example, it can be seen from the local enlarged figure in Fig. 3 (the picture in the red box) that the amplitude difference between the two sensors at the head and tail of beech is about 6 times, so simply setting a fixed threshold does not work for all P-waves.

However, as can be seen from Fig. 3, although the amplitude of P-wave is much smaller than that of S-wave, the amplitude of P-wave at the time of arrival is still significantly larger than that of noise signal. Therefore, this paper determined the threshold h according to the difference between P-wave amplitude and noise amplitude, that is, the time when the amplitude of AE waveform was *h* times greater than the maximum amplitude of noise for the first time was recorded as the arrival time of P-wave (corresponding to FIND(.) function in Fig. 4). However, there are still small differences in the angle and strength of each PLB test, which will inevitably lead to significant differences in the amplitude of P-wave in different independent tests. In order to overcome the randomness caused by PLB tests, an adaptive threshold setting method was adopted in this paper. That is, starting from the initial threshold h_0, the threshold was gradually increase in a certain step Δh to the maximum threshold h_{max}, and the P-wave velocity v^k_{ij} was calculated corresponding to different thresholds using the TDOA location method:

$$v^k_{ij}=d_{ij}/\Delta t_{ij} \qquad (3)$$

where: d_{ij} is the distance from the i^{th} sensor to the j^{th} sensor; Δt_{ij} is the time difference between the P-wave reaching the i^{th} sensor and the j^{th} sensor calculated according to TDOA; i,j = 1,2,3,4,5 。 k=1,...,k_{max}， $k_{max}=(h_{max}-h_0)/\Delta h$。

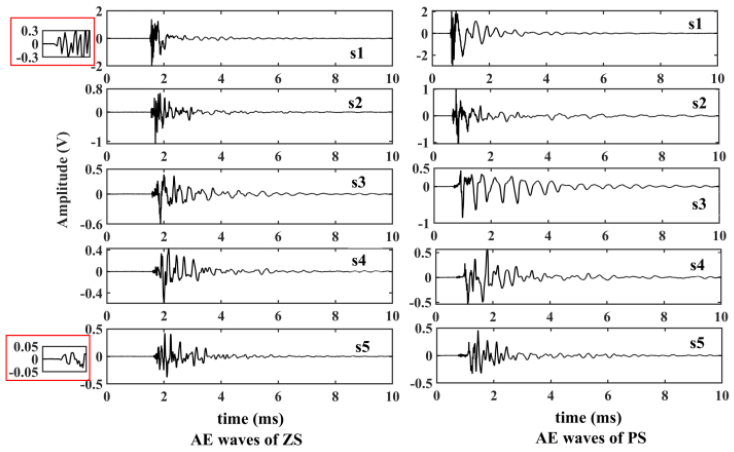

Fig. 3: Original AE signal collection from 5 different sensors.

In fact, the difference of PLB test can not affect the propagation velocity of P-wave. Therefore, the standard deviation was calculated respectively according to the k_{max} groups velocities calculated under different thresholds, as shown in Fig. 4 and Fig. 5 as function STD (.). Then the group of velocities with the smallest standard deviation was taken as the velocities measured in this independent test, the velocities obtained from all 15 independent tests were recorded, the average value was taken as the final velocity of v_{ij} (corresponding to v_{av} line in Tab. 1), then the average value of this line was recorded as the velocity of P-wave (corresponding to v_p in Tab. 5). In order to be distinguished, the improved TDOA was called TDOA method with adaptive threshold, which was recorded as TDOA_ah (as shown in the dotted box in Fig. 4), the complete P-wave velocity calculation process is shown in Fig. 4.

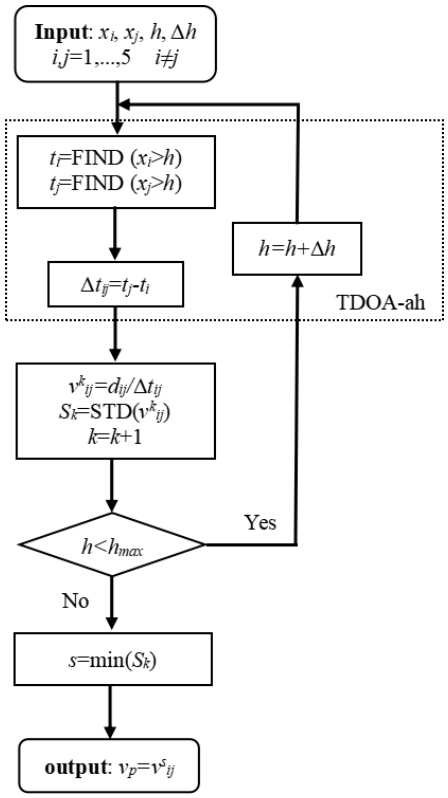

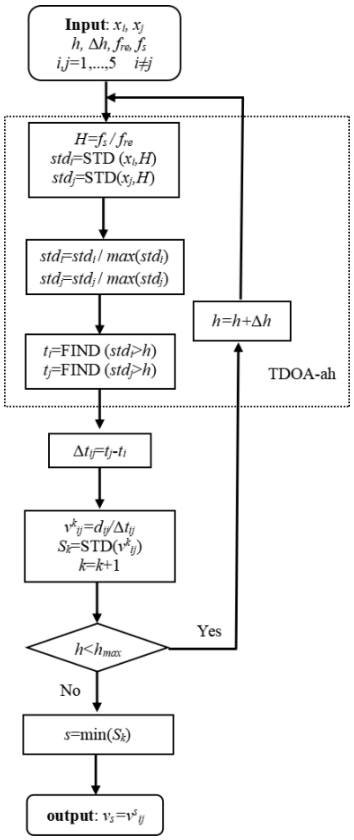

Fig. 4: The calculation flow chart of P wave. *Fig. 5: The calculation flow chart of S wave.*

S-wave velocity calculation based on improved TDOA algorithm

Li et al. (2018, 2020, 2021) used the method of signal correlation analysis to calculate the time difference of AE signals arriving at different sensors, that is, the time corresponding to the maximum correlation coefficient was taken as the time difference. Because there are a large number of standing wave components in AE signal waveform, these standing wave components have a significant impact on signal correlation analysis. For example, for two AE signals s2 and s3 with a length of 2 ms in the same PLB test (as shown in the top two boxes in Fig. 6), when performing correlation analysis directly, although the time when the correlation coefficient is the largest (as pointed A in Fig. 6) can be determined, there are a large number of points very close to the amplitude of A in a small range (in the red circle in Fig. 6). In other words, it is reasonable to use any point within this range to determine the time difference. But when different points are selected for calculation, there is a significant difference in the velocity. For example, the velocities calculated by selecting point A and point B are 926 $m.s^{-1}$ and 1154 $m.s^{-1}$ respectively. In response to this dilemma, Li et al. (2018, 2020, 2021) used high pass filtering to remove the standing wave component from the original AE signal. According to the corresponding frequency characteristics of the AE sensor, the cut-off frequency f_c of the filter was usually set to 22 kHz. After correlation analysis of the filtered two signals, it is easy to determine the time difference (as shown at the bottom and middle of Fig. 6). However, there is still a lack of sufficient basis for the setting of cut-off frequency. In fact, different cut-off frequencies can cause great changes in TDOA, resulting in significant differences in the calculated velocity. Fig. 6 shows that when the cut-off frequency f_c is set to 15 kHz, 22 kHz and 45 kHz, the time difference values are 0.110 ms, 0.086 ms and 0.130 ms respectively, and the calculated velocities are 1364 $m \cdot s^{-1}$, 1744 $m \cdot s^{-}1$ and 1154 $m \cdot s^{-1}$ respectively.

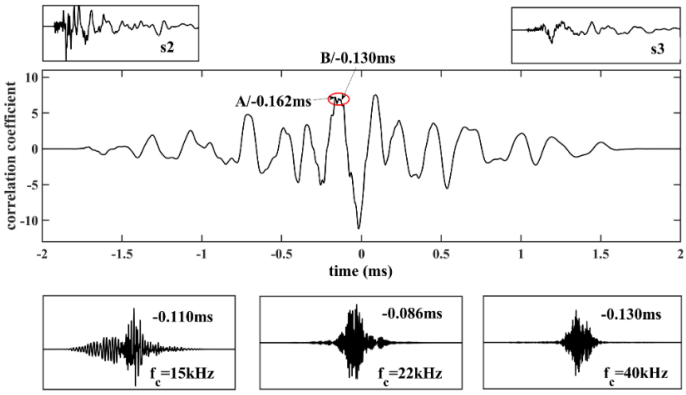

Fig. 6: The effect of cutoff frequency on the arrive time of S-wave.

In view of the shortcomings of correlation analysis method, this paper proposed an improved TDOA method for calculating S-wave TDOA on the basis of referring to TDOA method in P-wave. According to the elastic wave theory, although S-wave propagates slower than P-wave, its amplitude is significantly higher than P-wave. Therefore, the time when the amplitude changes suddenly after P-wave can be recorded as the arrival time of S-wave. However, due to the superposition of different frequency waveforms, it is not easy to directly

find the arrival time of S-wave from the original waveform (in the upper of Fig. 7). According to the statistical principle, the sudden change of signal amplitude means that the standard deviation of signal amplitude distribution will change significantly in a certain interval. Therefore, this paper used the method of signal standard deviation to calibrate the arrival time of S-wave. The specific method was to continuously intercept the data by moving the window with fixed length D on the original AE signal, and calculated the standard deviation s for each intercepted data (recorded as STD(.) function in Fig. 5), and normalized it. Then the arrival time difference of S-wave was determined by setting the threshold according to the requirements of TDOA method. Fig. 7 shows that when the threshold h is set to 0.2, the arrival time difference of S-wave is 0.162 ms, on the contrary, when h is greater than 0.2, it is 0.170 ms. Like the processing of P-wave, in order to avoid the irrationality of fixed threshold setting, the threshold was adaptively varied in steps of Δh over the range of h_0 to h_{max}, and a group of velocities with the minimum standard deviation were also taken as the final S-wave velocities. The complete S-wave velocity calculation process is shown in Fig. 5.

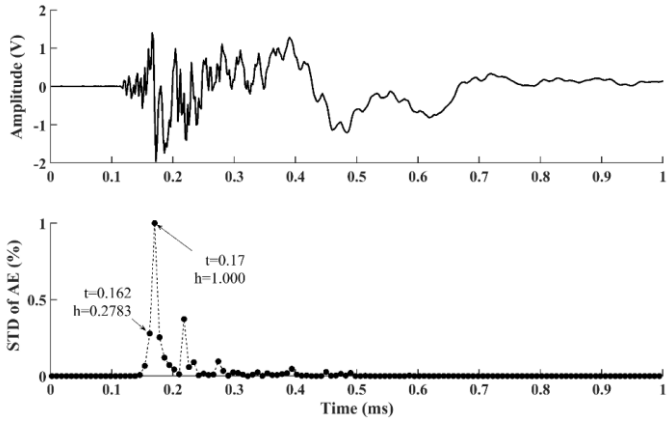

Fig. 7: The standard deviation of S wave.

RESULTS AND DISCUSSION

Propagation velocities of P and S waves

In calculating the propagation time difference of AE signals using the TDOA method, the response speed of different sensors to AE signals can directly affect the stability of velocity calculation (Zhou et al. 2021). In order to minimize the influence of sensors on velocity calculation, this paper used the AE signals collected by any two sensors to calculate the velocities of P-wave and S-wave (v_{ij},i,j = 1,2,3,4,5), and then took the average value of these 10 velocities as the final propagation velocity. When calculating the P-wave velocity, the thresholds of h_0 and h_{max} were set to 1 and 10 and the step size was 0.1 respectively; when calculating the S-wave velocity, the thresholds of h_0 and h_{max} were set to 0 and 1 respectively, and the step size was 0.05.

As can be seen from Tab. 1, TDOA_ah algorithm was used for each independent PLB test to find the best threshold adaptively when calculating P-wave velocity. In the test of ZS specimen, the standard deviation varied from 29.0 $m \cdot s^{-1}$ to 338.7 $m \cdot s^{-1}$, and the corresponding relative error varied from 0.62% to 7.21%. In the test of PS specimen, the standard deviation

varied from 44.5 m·s^{-1} to 335.3 m·s^{-1}, and the corresponding relative error varied from 6.68% to 7.21%. Finally, after averaging the third row from the bottom in the two tables, the propagation velocities of P-wave in ZS and PS were 4701 m·s^{-1} and 5021 m·s^{-1} respectively. Because the P-wave mainly propagates along the wood fibers of the test piece, and the wood fibers of PS are more neatly arranged (Fig. 8), which is more conducive to P-wave propagation, and the wood fibers of soft wood are longer than those of hardwood wood (Lamy et al. 2015), resulting in faster propagation velocity of PS than ZS.

Tab. 1: Propagation velocities of P-wave in ZS specimen.

NO.	v_{12}	v_{13}	v_{14}	v_{15}	v_{23}	v_{24}	v_{25}	v_{34}	v_{35}	v_{45}
1	5000	4839	4592	4615	5000	4839	4592	5000	4688	4688
2	5000	4839	4592	4615	4412	4412	4500	4688	4688	5000
3	5000	4839	4688	4615	4688	4688	4500	4688	4545	5000
4	4688	4839	4592	4615	5000	4688	4592	4688	4688	4688
5	5000	4688	4688	4615	4688	4688	4688	5000	4688	4688
6	5000	4839	4592	4615	4412	4412	4500	4688	4688	4688
7	5000	4839	4688	4615	5000	4688	4592	4688	4412	5000
8	5000	4839	4592	4615	4688	4688	4688	4167	4688	5000
9	5000	4839	4688	4545	5000	4839	4500	5000	4545	4412
10	5000	4839	4688	4615	4688	4688	4500	4688	4412	5000
11	5000	4545	4592	4615	4688	4412	4688	4688	4688	5000
12	5000	4839	4787	4545	4688	4688	4500	4688	4545	4412
13	5000	4839	4592	4545	5000	4688	4412	5000	4286	3750
14	5000	4839	4787	4615	4688	4688	4688	4688	4688	4688
15	5000	4839	4688	4615	4688	4688	4592	4688	4545	4688
v_{av}	**4979**	**4809**	**4656**	**4601**	**4755**	**4653**	**4569**	**4736**	**4586**	**4668**
s	80.7	82.7	70.3	29.0	202.2	135.1	89.3	211.5	130.9	338.7
h	5.5	2.9	2.9	3.1	5.9	5.7	4.3	5.5	3.9	4.9

Tab. 2: Propagation velocities of P wave in PS specimen.

NO.	v12	v13	v14	v15	v23	v24	v25	v34	v35	v45
1	5000	5172	5114	4918	5769	5172	5000	5000	4839	4688
2	4412	5000	5000	4918	5769	5172	5114	5000	4839	5000
3	4167	5000	5000	4762	6250	5172	5233	5000	5172	4167
4	5000	5172	5114	5000	5357	5172	5114	5000	4839	4688
5	5000	5000	5114	4762	6250	5172	4688	5357	4545	4688
6	5000	5172	5114	5000	5357	5172	5000	5000	4839	4688
7	5000	5000	4787	4688	5769	5000	4787	5357	4545	5000
8	4688	5000	5000	5000	6250	5172	5114	5000	4545	5000
9	5000	5172	5000	4839	5769	5172	5114	4688	4545	4688
10	4688	5000	4891	4615	5769	5172	4688	5357	4286	4412
11	5000	5172	5114	5000	5769	5172	5000	5357	4688	5357
12	4688	5000	5000	4762	6250	5172	5000	5357	4545	5000
13	4412	5000	4891	4918	5769	5172	5114	4688	5000	5000
14	4412	5172	4787	5172	6250	5172	4891	5000	4412	4688
15	4688	4839	4891	4918	5357	5172	5000	5000	4167	5000
vav	4743	5058	4988	4885	5847	5161	4990	5077	4654	4804
s	284.9	104.7	116.0	146.2	335.3	44.5	162.5	230.4	269.5	290.1
h	2.7	5.1	2.7	2.7	5.5	5.9	3.5	5.9	3.7	5.7

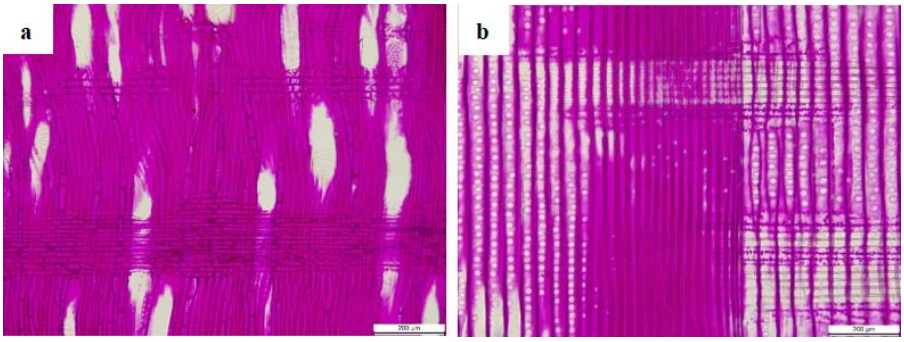

Fig. 8: Radial microstructures of Zelkova schneideriana and Pinus sylvestris Mongolicas Litv.

For each independent PLB test, TDOA_ah algorithm can also find the best threshold adaptively when it is used to calculate the S-wave velocity. In the test of ZS specimen, there was a large standard deviation when calculating the velocity according to the three signals s3, s4 and s5 furthest from the AE source. Nevertheless, their evaluation velocity value was still within a reasonable range. On the contrary, the calculation of S-wave velocity in the test of PS specimen was very stable. Similarly, the propagation velocities of S-wave in ZS and PS were1700 $m.s^{-1}$ and 1339 $m.s^{-1}$ respectively. Existing studies show that the transverse wave velocity increases with increasing density in geotechnical soils (Wang et al. 2019), geotechnical soils have similar viscoelastic and porous characteristics with wood. The density of ZS in this paper is approximately twice that of PS, so it can be assumed that the difference in S-wave velocity is mainly caused by the density of the material.

After obtaining the propagation velocity of AE signal P-wave in two kinds of specimens, this paper used the P-wave velocity to estimate the young's moduli of the specimens:

$$E = v_p^2 \cdot \rho \tag{4}$$

At the same time, in order to verify the effect of estimation, dumbbell shaped small specimens were made according to the test method GB / T 1938-2009 for tensile strength along the grain of wood. The young's moduli of elasticity of PS and ZS specimens were tested by tensile test on Shimadzu AG-X100 kN electronic universal material testing machine, and the test specimen was made as shown in Fig. 9.

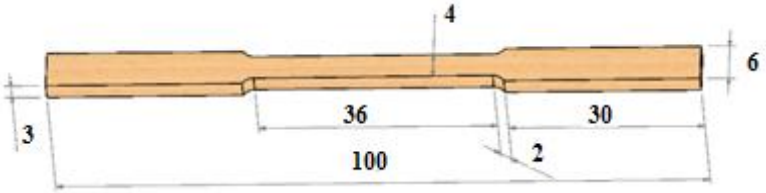

Fig. 9: Schematic diagram of tensile test piece. (Units in mm).

The Young's moduli of ZS and PS samples estimated by P-wave is 12.6 GPa and 9.4 GPa respectively, while that measured by tensile test is 15.4 GPa and 9.5 GPa respectively. The results showed that for the PS specimen, the estimated and measured Young's moduli were completely consistent, and the young's modulus of the ZS specimen estimated by P-wave was slightly lower than the measured value of the test.

Energy attenuation mode of AE signal

The energy **a**ttenuation law and the propagation velocity of AE signal are the key basis for the application of AE Technology (Michalcová et al. 2018). Li et al. (2021) studied the energy attenuation law of AE signal propagating in PS and ZS specimens by internal longitudinal wave (ILW) and surface transverse wave (STW) through different test methods. The results showed that the energy of ILW and STW decayed exponentially, and there was no obvious difference in the attenuation process in different specimens. In fact, in all tests, the AE signal obtained by each sensor includes longitudinal wave, transverse wave and standing wave components. In particular, the amplitude of standing wave component is large and lasts for a long time, which is the main part of AE signal waveform energy. Objectively speaking, it is difficult to accurately separate P-wave, S-wave and standing wave components from an AE waveform. For the application of AET, it is more meaningful to study the attenuation characteristics of AE signals with different frequencies. Therefore, this paper first removed the influence of the standing wave component by intercepting the signal, that is, intercepting the signal with a length of 0.5ms from the arrival time of P-wave to study the law of energy attenuation. Then, through the method of 4-layer wavelet decomposition, the energy attenuation law of AE signals with different frequencies was studied for the detail of each layer. Because the standing wave component was completely contained in the approximations of wavelet decomposition, it is not necessary to consider the influence of standing wave here. Finally, the energy **a**ttenuation models of AE signals in different frequency bands were obtained by data fitting.

MATLAB R2018b software was used for AE signal energy calculation and analysis. When performing 4-layer wavelet decomposition on the original AE signal, daubechies 10 orthogonal wavelet function was selected as the wavelet kernel, and the decomposed 4-layer details were recorded as 1stlayer, 2ndlayer, 3rdlayer and 4th layer respectively. The main frequencies of these 4 signals were the same for both PS and ZS specimens (Figs.10 and 11). Because there were some differences in the amplitude of AE signal in each independent PLB test, the ratio was used to describe the AE signal energy, that is, the energy of s1 signal was regarded as 100%, and the energy of the other four AE signals was the ratio relative to the signal energy.

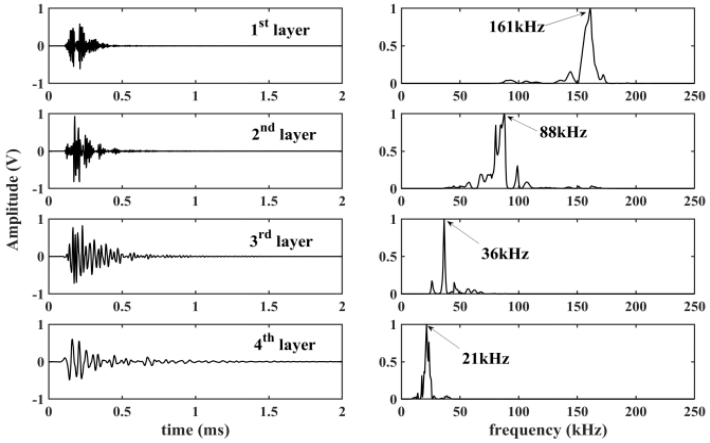

Fig. 10: Waves and spectra of four detail signals in ZS specimen.

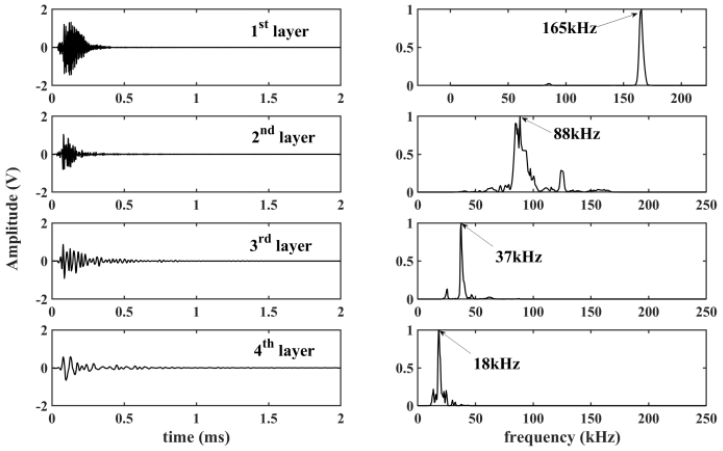

Fig. 11: Waves and spectra of four detail signals in PS specimen.

Through exponential function fitting, the energy **a**ttenuation models of AE signal in PS and ZS are obtained as follows:

$$y_{ZS} = e^{-10.89x} \quad (5)$$

$$y_{PS} = e^{-17.30x} \quad (6)$$

where: y_{ZS} and y_{PS} are the energy attenuation functions of AE signals on ZS and PS specimens respectively; x is the propagation distance, and the position of sensor s1 is taken as the coordinate origin.

The fitting curve in Fig. 11a shows that the AE signal decays faster in PS than in ZS. In addition to the difference of microstructure, the smaller density of PS specimen is the main factor leading to the faster decay of AE signal energy.

For the 4-layer detail signal after wavelet decomposition, the fitting curves of energy attenuation in ZS and PS specimens are shown in Figs. 11b,c respectively. It can be seen from these two figures that in the two specimens, the higher the frequency, the faster the component energy attenuation. For the 1st layer signal whose dominant frequency is about 160 kHz, the signal energy attenuated faster in ZS. But the energy attenuation rate of 2nd layer and 3rd layer signals in PS specimen is significantly higher than that in ZS specimen, and it is the same with the 4th layer signal in the two specimens. Therefore, the overall performance is that the energy attenuation is faster in PS specimen.

The energy attenuation fitting model of different frequency components of the AE signal in the ZS specimen is as follows:

$$\left.\begin{aligned} y_{ZS,1} &= e^{-28.69x} \\ y_{ZS,2} &= e^{-9.77x} \\ y_{ZS,3} &= e^{-7.67x} \\ y_{ZS,4} &= e^{-6.11x} \end{aligned}\right\} \quad (7)$$

where: $y_{ZS,i}$, i =1,2,3,4, is the energy attenuation function of the i[th] layer detail signal on the ZS specimen after wavelet decomposition.

Similarly, the energy attenuation fitting model of different frequency components of AE signal in PS specimen is as follows:

$$\left.\begin{aligned} y_{ZS,1} &= e^{-28.69x} \\ y_{ZS,2} &= e^{-9.77x} \\ y_{ZS,3} &= e^{-7.67x} \\ y_{ZS,4} &= e^{-6.11x} \end{aligned}\right\} \quad (8)$$

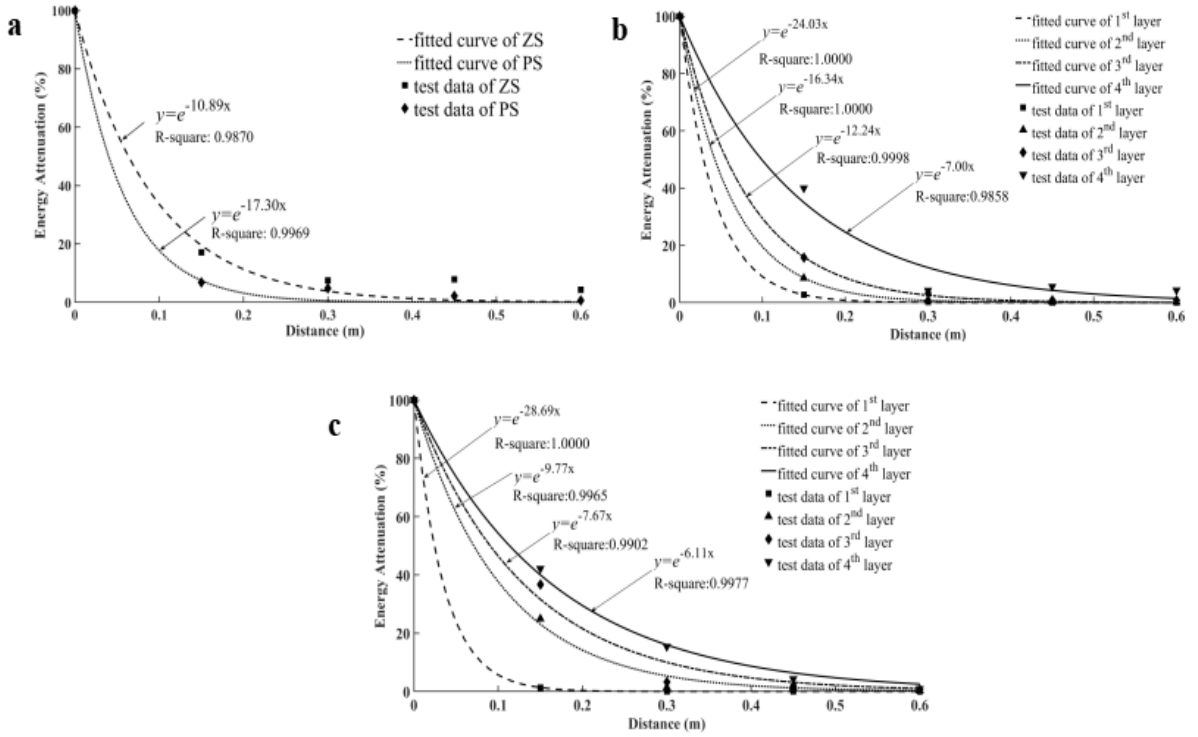

Fig. 12: Fitted energy attenuation curve: a) Fitted curves of original AE signals for PS and ZS specimen, b) Fitted curves of different frequency components in ZS specimen, c) Fitted curves of different frequency components in PS specimen.

CONCLUSIONS

In this paper, the propagation characteristics and energy attenuation process of AE signal in PS and ZS specimens were studied. The results showed that because the wood fiber in PS was longer, P-wave propagated faster in PS specimens. The propagation velocity of S-wave depends more on the density of wood, so the propagation velocity in ZS was significantly higher than that in PS. Compared with the experimental test, it was found that the young's modulus of elasticity of the wood can be estimated accurately by the velocity of P-wave. AE signal decayed faster in PS, and the energy decayed faster with the increase of signal frequency; however, the component with the highest frequency decayed faster in ZS. In the future, the research results of this paper are planned to be used in the localization and damage detection of AE sources in wood.

ACKNOWLEDGEMENTS

The authors are grateful for the support of the National Natural Science Foundation of China (No. 32160345， No. 31760182); Department of Education of Yunnan Provincial (No.2021Y224, No.2021J0156, No.2021J0158) and Start-up fund for introducing talents and scientific research of Anhui University of Engineering (NO: 2021YQQ037).

REFERENCES

1. Aguilera, A., Vega, M., Méausoone, P.J., 2007: Effects of grain angle on the amplitudes of acoustic emission and surface roughness in wood machining. Wood Science and Technology 41(4): 373–381.
2. Aicher, S., Hofflin, L., Langer, G.D., 2001: Damage evolution and acoustic emission of wood at tension perpendicular to fiber. Holz als Roh- und Werkstoff 59: 104-116.
3. Ando, K., Hirashima, Y., Sugihara, M., Hirao, S., Sasaki, Y., 2006: Microscopic processes of shearing fracture of old wood, examined using acoustic emission technique. Journal of Wood Science 52: 483-489.
4. Bertolin, C., Ferri, L., Razavi, J., Berto, F., 2020: Acoustic emission NDT for monitoring hygro-mechanical reactions of coated pine wood: a methodological approach. Procedia Structural Integrity 28: 208-217.
5. Chen, Z., Gabbitas, B., Hunt, D., 2006: Monitoring the fracture of wood in torsion using acoustic emission. Journal of Materials Science 41: 3645-3655.
6. Hu, W.G., Zhang, J.L, 2022: Effect of growth rings on acoustic emission characteristic signals of southern yellow pine wood cracked in mode I. Construction and Building Materials 329: 127092.
7. Lamy, F., Takarli, M., Angellier, N., Dubois, F., Pop, O., 2015: Acoustic emission technique for fracture analysis in wood materials. International Journal of Fracture 192(1): 57-70.
8. Li, M., Wang, M.H., Ding, R., Deng, T.T., Fang, S.Y., Lai, F., Luo, R.H., 2021: Study of acoustic emission propagation characteristics and energy attenuation of surface transverse wave and internal longitudinal wave of wood. Wood Science and Technology 55: 1619-1637.
9. Li, X.C, Ju, S., Luo, T.F, Li, M., 2020: Effect of moisture content on propagation characteristics of acoustic emission signal of *Pinus massoniana* Lamb. European Journal of Wood and Wood Products 78: 185–191.
10. Li, Y., Xu, F.Y., 2019: Signal processing and identification on the surface of *Pinus massoniana* Lamb. glulam using acoustic emission and improvement complete ensemble empirical mode decomposition with adaptive noise. Measurement 148: 106978-106978.

11. Li, Y., Yu, S.S., Dai, L., Luo, T.F., Li, M., 2018: Acoustic emission signal source localization on plywood surface with cross-correlation method. Journal of Wood Science 64: 78-84.
12. Michalcová, L., Bělský, P., Petrusová, L., 2018: Composite panel structural health monitoring and failure analysis under compression using acoustic emission. Journal of Civil Structural Health Monitoring 8(4): 607-615.
13. Nasir, V., Cool, J., 2018: A review on wood machining: characterization, optimization, and monitoring of the sawing process. Wood Material Science and Engineering 15(3): 1–16.
14. Nasir, V., Cool, J., 2020: Characterization, optimization, and acoustic emission monitoring of airborne dust emission during wood sawing. International Journal of Advanced Manufacturing Technology 109: 2365–2375.
15. Nasir, V., Cool, J., Sassani, F., 2019: Acoustic emission monitoring of sawing process: artificial intelligence approach for optimal sensory feature selection. The International Journal of Advanced Manufacturing Technology 102: 4179–4197.
16. Nasir. V., Nourian, S., Avramidis, S., Cool, J., 2019a: Stress wave evaluation by accelerometer and acoustic emission sensor for thermally modified wood classification using three types of neural networks. European Journal of Wood and Wood Products 77(1): 45–55.
17. Ohuchi T, Hermawan A, Fujimoto N. ,2011: Basic Studies on Fracture Toughness of Sugi and Acoustic Emission. Journal of the Faculty of Agriculture Kyushu University 56: 99-102.
18. Pallarés, F.J., Betti, M., Bartoli, G., Pallarés, L., 2021: Structural health monitoring (SHM) and Nondestructive testing (NDT) of slender masonry structures: A practical review. Construction and Building Materials 297: 123768.
19. Reiterer, A., Stanzl-Tschegg, S.E., Tschegg, E.K., 2000: Mode I fracture and acoustic emission of softwood and hardwood. Wood Science & Technology 34(5): 417-430.
20. Ritschel, F., Brunner, A.J., Niemz, P., 2013: Nondestructive evaluation of damage accumulation in tensile test specimens made from solid wood and layered wood materials. Composite Structures 95(1): 44-52.
21. Ritschel, F., Yang, Z., Brunner, A.J., Fillbrandt, T., Niemz, P., 2014: Acoustic emission analysis of industrial plywood materials exposed to destructive tensile load. Wood Science & Technology 48(3): 1-21.
22. Sun, J.P., Hu, Y.C., Wang, F.H., 2013: Study on quantitative nondestructive test of wood defects based on intelligent technology. Chinese Journal of Scientific Instrument 34(9): 1955–1960.
23. Sun, J.P., Wang, F.H., Zhu, X.D., 2008: Application of wavelet-neural network in defect location non-destructive testing of MDF. Chinese Journal of Scientific Instrument 29(5): 954–958.
24. Wang, M.H., Deng, T.T., Ju, S., Li, X.C., Li, X.S., Li, M., 2020: Effect of wood surface crack on acoustic emission signal propagation characteristics. Journal of Northeast Forestry University 48(10): 19–25.

25. Wang, Y., Xu, X.K, Zhang, Y.G., 2012: Characteristics of P-wave and S-wave velocities and their relationships with density of six metamorphic kinds of coals. Chinese Journal of Geophysics- Chinese Edition 55(11): 3754-3761.
26. Wu, Y., Perrin, M., Pastro, M.L., Casari P., Gong X.J., 2021: On the determination of acoustic emission wave propagation velocity in composite sandwich structures. Composite Structures 259: 113231.
27. Zhou, Z.L., Rui, Y.C., Cai, X., Lu, J.Y., 2021: Constrained total least squares method using TDOA measurements for jointly estimating acoustic emission source and wave velocity. Measurement 182: 109758.

SAIYIN FANG, CHANG LIN HUANG, TINGTING DENG, KUN DU
SOUTHWEST FORESTRY UNIVERSITY
SCHOOL OF MACHINERY AND TRANSPORTATION
BAILONG ROAD 300, PANLONG DISTRICT
KUMMING
CHINA

MING LI[1,2*]
[1]KEY LABORATORY OF ADVANCED PERCEPTION AND INTELLIGENT CONTROL OF HIGH-END EQUIPMENT OF MINISTRY OF EDUCATION
[2]ANHUI POLYTECHNIC UNIVERSITY
SCHOOL OF ELECTRICAL ENGINEERING
BEIJING MIDDLE ROAD
WUHU
CHINA
*Corresponding author: swfu_lm@swfu.edu.cn